Hole Mobility in Nanocrystal Solids as a Function of Constituent Nanocrystal Size

ARTICLE *in* JOURNAL OF PHYSICAL CHEMISTRY LETTERS · OCTOBER 2014

Impact Factor: 7.46 · DOI: 10.1021/jz5015086

THE JOURNAL OF PHYSICAL CHEMISTRY Letters

Letter

pubs.acs.org/JPCL

Hole Mobility in Nanocrystal Solids as a Function of Constituent Nanocrystal Size

Nuri Yazdani, Deniz Bozyigit, Olesya Yarema, Maksym Yarema, and Vanessa Wood*

Laboratory for Nanoelectronics, Department of Information Technology and Electrical Engineering, ETH Zürich, Gloriastrasse 35, Zürich CH-8092, Switzerland

Supporting Information

ABSTRACT: Solids of semiconductor nanocrystals (NCs) are semiconductors in which the band gap can be controlled by changing the size of the constituent NCs. To date, nontrivial dependencies of the carrier mobility on the NC size have been reported. We use the time-of-flight (TOF) technique to measure the carrier mobility as a function of the NC size and find that the hole mobility of the NC solid increases dramatically with decreasing NC radius. We show that this result is in agreement with an analytic model for carrier mobility in NC solids. We further implement Monte Carlo simulations to aid in understanding the transient measurements in the context of models of dispersive transport. This work highlights that changing NC size in a device has important implications for charge transport.

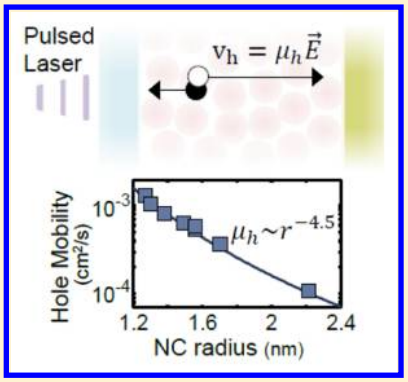

SECTION: Physical Processes in Nanomaterials and Nanostructures

Films of semiconductor nanocrystals (NC solids) hold great promise as low-cost, solution-processable semiconductors with electronic and optical properties that can be tuned by varying the size and composition of the constituent NCs, as well as their surface-terminating ligands.[1] To date, research has largely focused on the influence of ligand length and composition on the electronic coupling between neighboring NCs,[2−5] which has a large impact on the charge transport in NC solids.[6,7] Changing the size of the constituent NCs is primarily considered a way to change the semiconductor band gap; here, we examine the implications of changing NC size on the carrier mobility, μ, which is defined from the drift velocity, $\vec{v}$, at which an electron or hole travels in an electric field, $\vec{v}_{e/h} = \mu_{e/h}\vec{E}$, and is a critical parameter in semiconductor device engineering.

Recently, theoretical calculations have predicted that, assuming that the inter-NC spacing in a NC solid remains the same, as the size of the constituent NC decreases, the mobility should increase.[6] This stems from the fact that decreasing NC size increases the kinetic energy of a carrier on a NC, reducing the effective energy barrier between NCs seen by the carrier. This enhances the leakage of the wave function outside of the NC, increasing the coupling between neighboring NCs.

To experimentally study the impact of NC size on carrier mobility, we turn to time-of-flight (TOF) photocurrent measurements, which have been shown to provide reliable measurements in low-mobility materials such as amorphous semiconductors,[8−11] organic semiconductors,[12,13] and NC-based solids.[14] Here, we first review the TOF technique and present results of Monte-Carlo-based simulations of TOF photocurrent measurements that enable us to understand how to correctly size the thickness of the semiconductor layer in our devices and interpret the results of our TOF measurements on NC-based solids. We then use TOF to investigate the hole mobility in PbS NC solids as a function of NC size and compare our experimental results to theory.

In TOF photocurrent measurements, the material under study is sandwiched between two contacts, which are fixed at a given potential, V_0, with respect to one another. A short laser pulse generates a charge distribution in the material at one of the contacts, and the resulting displacement current transient is measured (see Figure 1a).

We perform the TOF measurements in the heterojunction architecture shown in Figure 1b that is commonly used for NC-based solar cells[15,16] where the PbS NC solid with 1,2-ethanedithiol (EDT) ligands is sandwiched between transparent fluorinated tin oxide (FTO)/titania and molybdenum oxide (MoO_x)/gold(Au) as the electron and hole extracting contacts, respectively. Devices are made using NCs with radii ranging from 1.2 to 2.1 nm (and corresponding optical band gaps ranging from 1.67 to 0.99 eV). Transmission electron microscope (TEM) images and absorption data of the NCs are given in the Supporting Information. Thicknesses of the PbS NC solid layers are optimized individually for each NC size based on the criteria explained below. While the devices have NC solid film thicknesses well above the optimum for a high

Received: July 18, 2014
Accepted: September 23, 2014
Published: September 23, 2014

   dx.doi.org/10.1021/jz5015086 | J. Phys. Chem. Lett. 2014, 5, 3522−3527

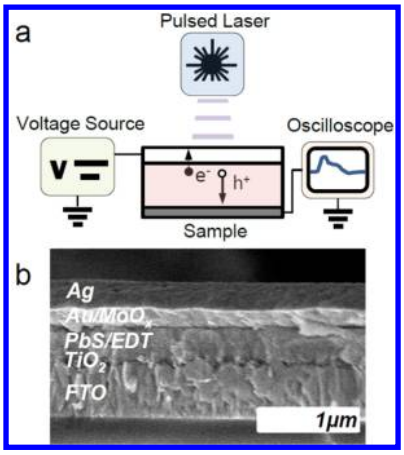

Figure 1. (a) Experimental setup of the TOF photocurrent measurement setup. (b) SEM of a cross section of one of the devices used in this work.

power conversion efficiency (PCE) solar cell, they exhibit PCEs of 1−4% and show rectifying behavior in the dark. Physical, electrical, and solar cell characterization for each device used in this work is given in the Supporting Information.

In TOF photocurrent transient measurements, the devices are illuminated through the FTO/titania using a picosecond pulsed laser to stimulate the transient photocurrent. With voltages of 1−9.5 V, electric fields in the range of 50−200 kV/cm are applied to the device such that electrons are extracted through the titania/FTO and holes travel through the PbS NC solid to the MoO_x/Au electrode. This means that the charge carriers arrive at the contacts through which they can be efficiently extracted, preventing a buildup of charge in the PbS NC solid layer, which could screen the applied field. Further, the selective FTO/titania and MoO_x/Au electrodes block back injection of charge into the PbS NC solid layer from the contacts (i.e., holes from FTO/titania).[17] This minimizes the recombination of photoinjected charges with charges injected from the contacts, and the small reverse bias currents ensure that the potential difference between the two contacts is held at V_0. Thus, the solar cell architecture facilitates the TOF photocurrent transient measurement.

To understand how to correctly size the PbS NC solid thickness for the TOF experiments and interpret the photocurrent transients, we simulate characteristic transients for three different types of semiconductor materials (Figure 2a). Details of the simulations are provided in the Supporting Information. The devices used in this study enable measurement of hole mobility; therefore, we discuss all concepts in terms of hole transport (indicated with the subscript, h); however, the analysis is equally valid for electron transport.

First, we consider the ideal case shown schematically in Figure 2b, where the semiconductor has an infinite absorption coefficient, α, such that all carriers are generated at the semiconductor−electrode interface and all holes travel with mobility μ through the semiconductor without trapping. As explained in the Supporting Information, the resulting current density transient, $J(t)$, is given by

$$J(t) = \frac{\sigma_s \mu V_0}{d^2} \qquad 0 < t < t_{tr} \tag{1}$$

where σ_s is the surface density of the sheet of charge moving between the electrodes and d is the thickness of the material. Such a transient is shown in Figure 2a. To calculate the hole mobility from a transient, one needs to determine the transit time (t_{tr}) for a given potential V_0

$$\frac{1}{t_{tr}} = \frac{\mu V_0}{d^2} \tag{2}$$

In this ideal case, the transit time t_{tr} is the time at which $J(t)$ drops abruptly to zero, corresponding to the time it takes the sheet of charge to reach the opposite electrode.

We next consider the case of a semiconductor where the carrier transport is ideal (i.e., all carriers have the same mobility and no trapping occurs) but where the absorption coefficient, α, is finite such that the electron−hole pairs will be generated at different distances within the material, as shown schematically in Figure 2c. The resulting transient is a superposition of the displacement currents generated by electrons and holes. However, by making the semiconductor sufficiently thick, it is possible to temporally separate the two currents. Because the initial distribution of both types of carriers after the laser pulse will be peaked at the illuminated electrode, if the semiconductor thickness is sized as $\alpha d \gg 1$, holes will have significantly more distance to traverse. Here, for each size of NC, initial devices are fabricated with thin layers, for which t_{tr} is not visible due to the overlap of the electron and hole transients. The layer thickness is progressively increased until t_{tr} can be discerned from the transients. The rounding of the

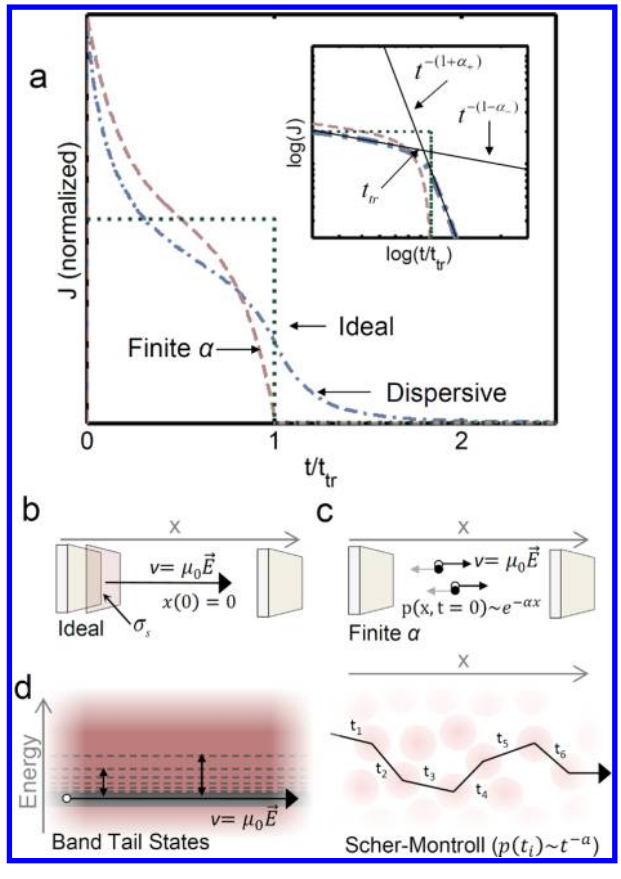

Figure 2. (a) Example TOF transients demonstrating ideal transport (dotted line), the effect of finite absorption (dashed line), and a transient with a large dispersion of transit times (dashed−dotted line). (b−d) Schematics of the physical processes, which would generate these different TOF transients.

dx.doi.org/10.1021/jz5015086 | J. Phys. Chem. Lett. 2014, 5, 3522−3527

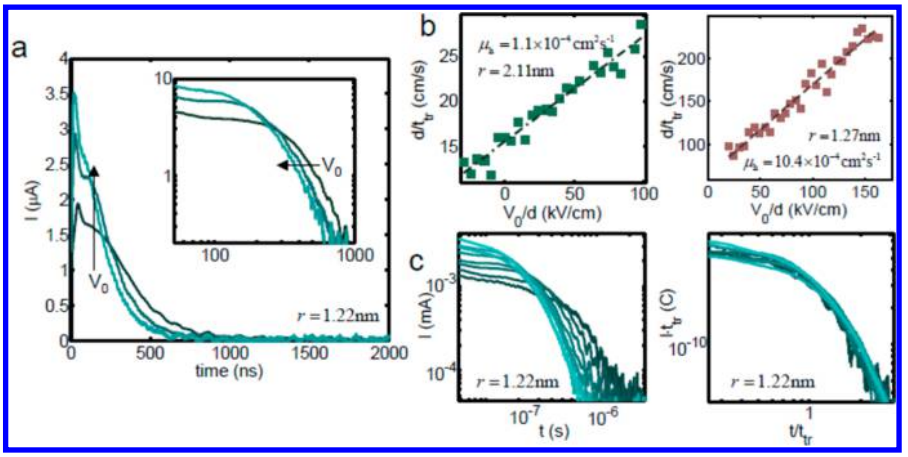

Figure 3. (a) Example TOF transients measured at bias voltages of 3, 5, and 7 V on a device incorporating NCs with a radius of 1.27 nm. The inset shows the data on a log−log plot around t_{tr}, where the power law behavior of the transients is visible. (b) Plots of d/t_{tr} versus V/d for two of the devices (left: NC radius of 2.11 nm; right: NC radius of 1.27 nm) exhibit good linearity. The characteristic hole mobilities (μ_h) are calculated from the slope of these plots. (c) The entire set of transients taken at voltages ranging from 0 to 9 V are plotted as measured (left) and after scaling the axes by t_{tr} (right) for the same device as that in (a).

shoulder of the current transient shown in Figure 2a results from the different distances that the holes traverse due to the finite absorption.

Finally, we consider the TOF photocurrent measurement for a low-mobility, disordered material in which transport is sometimes modeled by a multiple-trapping model, where an exponential distribution of localized states extends from an effective band, as shown schematically on the left of Figure 2d. A transient for this multiple-trapping model is plotted in Figure 2a. It is characterized by a shoulder occurring at $t = t_{tr}$ in a $\log(I)$ versus $\log(t)$ plot and transients at times before and after t_{tr} that follow distinct power laws

$$I^- \approx t^{-(1-\alpha_-)} \quad t < t_{tr}$$
$$I^+ \approx t^{-(1+\alpha_+)} \quad t > t_{tr} \tag{3}$$

indicating dispersion in the individual carrier transport times larger than that expected from the Gaussian broadening of a packet of charge due to diffusion. From t_{tr}, one calculates a characteristic drift velocity (v_h) with which a portion of holes traverse the device. In the multiple-trapping model picture, a distribution of shallow trap states extends from a band with mobility μ_0. The characteristic mobility, μ_h, computed from v_h is a measure of the free hole mobility, μ_0, and some contribution due to the band tail states that act as shallow traps. In the limit that a large fraction of carriers traverses the material without interacting with the band tail states, the characteristic mobility μ_h is an accurate estimate for the free hole mobility in the band μ_0. On the other hand, if each hole is trapped multiple times in the shallow band tail states during its transit, than μ_h is an underestimate of μ_0.

Charge transport in NC solids has been described not only in the multiple-trapping model picture described above[6,18−20] but also with variable range hopping models (Figure 2d).[21−24] The transients described by eq 3 exhibit what is referred to as anomalous dispersion.[9] The only requisite for anomalous dispersion is the existence of a long tail in the distribution of localization times, which is present in both the multiple-trapping model and the variable range hopping model.[25,26] The same transient in Figure 2a could be reproduced by assuming a power law distribution for the hopping times in the variable range hopping model.[27] In the variable range hopping model, the characteristic hole velocity (v_h) stems from percolative transit pathways through the NC solid with a narrow distribution of hopping times having a defined mean value. Thus, either model for charge transport in NC solids can be used to interpret TOF transient data.

Figure 3a shows an example set of TOF transients for the device with NCs of radius 1.22 nm. The presence of a clear shoulder is visible in the transients. The inset of the figure shows the same transients on a log−log plot, from which t_{tr} is determined from least-squares fits of the data over manually selected time windows. Plotting $d/(t_{tr})$ versus V_0/d and using eq 2 along with the PbS NC solid layer thickness, d, we compute the characteristic hole mobility μ_h. Such plots are shown for two devices in Figure 3b. The points remain linear over the wide range of V_0, and the mobility is found from the slope of a linear fit to eq 2. To check the reproducibility in the mobility measurement over a range of NC layer thicknesses, we measure μ_h for NCs of 1.56 nm in two devices with different NC layer thicknesses. Mobilities of $5.4 \pm 0.4 \times 10^{-4}$cm^2/s (for the 340 nm thick NC layer) and $5.8 \pm 0.2 \times 10^{-4}$cm^2/s (for the 430 nm thick NC-layer) are found, within error of one another. The hole mobility as a function of NC radius is summarized in Figure 4a. We find a strong dependence of mobility on NC radius that is fit by $\mu_h \approx r^{-\beta}$ with $\beta = 4.5 \pm 0.2$.

This trend of increasing mobility with decreasing NC size can be intuitively understood to result from the increased coupling between NCs of smaller sizes. Following the analytical approach of Shabaev et al.,[6] in Figure 4b and c, we plot hole wave functions in neighboring PbS NCs of radii $r = 2$ and 4 nm separated by a potential barrier of thickness $\delta = 6$ Å and height $U_0 = 1$. As the radii of the NCs increase, the confinement decreases, and less of the wave fuction leaks out of the NC, resulting in a decrease in coupling between neighboring NCs. This coupling directly influences the mobility. Again, following the model of Shabaev et al., which describes band transport by modeling a NC solid as a cubic superlattice of potential wells, we plot the calculated free hole mobility (μ_0) as a function of NC radius for different separations (δ) and barrier heights (U_0) between neighboring NCs. While varying U_0 and δ influences the magnitude of μ_0, the strong dependence of μ_0 on NC radius remains (Figure 4d). Figure 4a and d shows good agreement

dx.doi.org/10.1021/jz5015086 | J. Phys. Chem. Lett. 2014, 5, 3522−3527

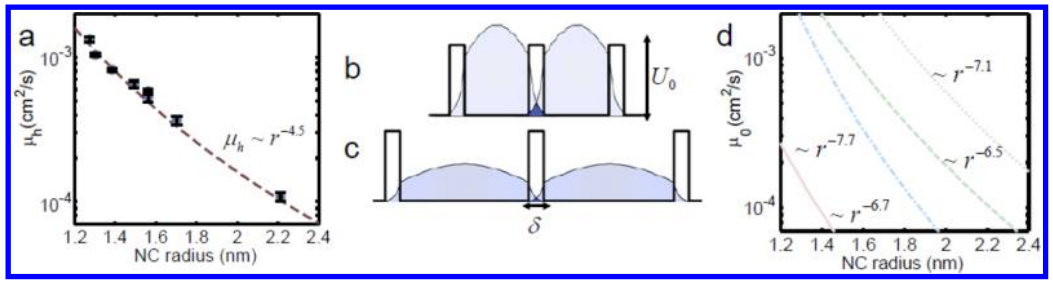

Figure 4. (a) Plot of the characteristic hole mobility (μ_h) extracted from the TOF photocurrent measurements versus NC radius (r). (b,c) Plots of the hole wave functions (blue shading) in two neighboring NCs separated by a barrier of width of δ = 6 Å and height of U_0 = 1 eV. Greater overlap of the wave functions is observed for the smaller NCs (b) than that for the larger NCs (c). (d) Free hole mobility (μ_0) versus r calculated for various NC−NC separations (δ) and barrier heights (U_0) showing the strong dependence of mobility on NC size. Parameters are as follows: for the solid line, δ = 4.5 Å and U_0 = 3 eV; for the dashed−dotted line, δ = 8.5 Å and U_0 = 1.2 eV; for the dashed line, δ = 4.5 Å and U_0 = 2 eV; and for the dotted line, δ = 6.5 Å and U_0 = 1.2 eV.

between the characteristic hole mobility measured experimentally with TOF and the analytical model for free hole mobility.

Our finding that carrier mobility increases with decreasing NC size, in agreement with theory, is in contrast to other carrier mobility measurements in NC solids, which have shown nontrivial or opposite dependences of the carrier mobility on NC size.[2−4] These studies, as most other studies of mobility in NC solids,[2,28−31] have been carried out in field effect transistor (FET) structures. Due to the presence of deep traps (i.e., traps that are more than a few kT away from the effective conduction or valence band) in NC solids,[18,32−35] FET measurements yield an effective mobility, which includes the contribution from carriers localized in deep trap states. If a larger fraction of charge carriers are trapped in NC solids composed of NCs with smaller size, the effective mobility could be measured to decrease with decreasing NC size, even if the free carrier mobility (μ_0) increases.[36]

As shown in the Supporting Information, in TOF measurements, the thermalization time from these deep traps is typically much longer than the transit time t_{tr} and therefore does not affect the position of t_{tr}.[37] While deep traps can capture mobile carriers and influence α_- (Figure S3, Supporting Information), we have observed that a small amount of background illumination enhances the signal-to-noise ratio of the TOF transient, without affecting the shape of the transient (Figure S4, Supporting Information). This enhanced signal could indicate a filling of the deep traps due to a shift in the quasi-Fermi levels. While the characteristic mobility found from TOF measurements is not influenced by the presence of deep traps, it can be affected by shallow traps. From the measurements presented here, it is not possible to determine to what extent, if any, the extracted characteristic mobility, μ_h, underestimates the free carrier mobility μ_0 due to shallow traps. In Figure 3c, we plot transients from one device for different V_0 on axes scaled by t_{tr}. A collapse of the transients onto one another is evident, which is a commonly observed feature in materials exhibiting anomalous dispersion.[9,13,27] In the context of the multiple-trapping model, this collapse suggests that the transport and trapping times scale in the same manner with V_0. As explained in the Supporting Information, with such scaling, ν_h will be linear with V_0 regardless of the average number of trapping events per carrier. In the future, with temperature-dependent measurements and the choice of an appropriate model, analyzing the form of the scaled transients can provide information on the energy distribution and density of the shallow trap states.[37]

In summary, our TOF measurements show that the characteristic carrier mobility strongly depends on the size of the NCs. In the case of PbS, a change in NC radius from 2.11 to 1.22 nm leads to a change in mobility of over an order of magnitude. Thus, by changing the size of the NCs to change the band gap, one also significantly changes the electronic transport. While the free carrier mobility and band gap are coupled parameters, it remains possible to tune the carrier mobilities in NC solids through control of the inter-NC spacing and barrier heights through proper ligand selection.

■ EXPERIMENTAL METHODS

Device Fabrication. Colloidal oleic-acid-capped PbS NCs were synthesized using the hot injection method, where size tunability is primarily achieved via different concentrations of oleic acid in the starting solution.[38] The NCs were washed three times in mixtures of ethanol and methanol and finally suspended in hexane. TEM images were acquired with a Philips CM12 electron microscope operating at 100 kV.

A titania nanoparticle paste (DSL 90-T, Dyesol), diluted to 125 mg/mL in acetone, was spun at 2500 rpm for 60 s on fluorinated tin oxide/glass substrates (Solaronix). Samples were placed on a hot plate at 500 °C for 60 min, then immersed in a 60 mM titanium tetrachloride/deionized water solution at 70 °C for 30 min, thoroughly rinsed with deionized water, and then placed on a hot plate at 500 °C for 60 min. PbS NC layers were deposited by sequential dipcoating in a PbS NC solution (5 mg/mL in hexane), a cross-linking solution (6 mM EDT in acetonitrile), and a rinsing solution (acetonitrile). The cross-linking and rinsing solutions use anhydrous acetonitrile, are stored and prepared in a N_2 glovebox, and are brought into ambient immediately prior to dip-coating. Dip-coating was carried out in air. To adjust the PbS NC solid thickness, the number of dip-coating cycles was varied, and the thicknesses were measured from SEM cross sections of the device following TOF measurements. The top MoOx/Au/Ag electrodes were deposited by thermal evaporation. Ag serves to improve the electrical contacts.

Measurements. Samples were mounted into a cryostat (Janis ST-500) after ∼2 min of air exposure, where they remained in vacuum during the measurements. $I-V$ measurements were carried out using a Keithley 2400 source measure unit, and AM1.5G illumination was provided by a mercury (xenon) DC arc lamp (Newport) and an air mass filter, calibrated using a piezoelectric sensor and an optical power meter (Thor Laboratories S302C, PM100D).

dx.doi.org/10.1021/jz5015086 | J. Phys. Chem. Lett. 2014, 5, 3522−3527

For the TOF measurements, the devices were mounted using a custom holder on a Nikon Eclipse Ti−U optical microscope. Background illumination of ∼2 mW/cm^2 was provided through a 10× objective lens by a red LED (Thor Laboratories M660L3-C3) driven by a Thor Laboratories Dc2100 LED driver, while the 405 nm, 100 ps excitation pulses were provided by a Hamamatsu picosecond pulsed laser (PLP-10). For some devices at low reverse bias, two sequential pulses separated by 5 ns were used to improve the signal-to-noise ratio. Voltage biases were applied using an Agilent 33522A arbitrary waveform generator, and the current was measured on a Rohde & Schwarz RTM1054 oscilloscope through the 50 Ω input. Measurements were averaged over 1024 cycles at a frequency of 10 kHz. We also note that despite finite times for disassociation of excitons on the individual NCs, these times scales are fast (on the order of ps in PbSe NCs[19]) compared to the time scale of the measurement and should not therefore affect the mobility values obtained.

Analytical Calculations. For the effective mass of holes in the NCs, we used the valence band effective mass in bulk PbS, neglecting nonparabolicity and using the average of m_{vl} and m_{vt} at 300 K taken from Preier,[39] while the electron rest mass was used in the barrier. The disorder parameter χ of the model was set to 10%. Values of δ between 4 and 8 Å were used as the nominal length of the EDT ligands used in device fabrication is ∼4 Å.[2]

■ ASSOCIATED CONTENT

Supporting Information

Analytical calculations regarding the TOF technique and interpretation of the extracted mobility, details of the simulations with a comparison of results for a sample with and without deep traps, physical and electrical characterization of the devices used in the study, and TOF measurements on a sample with and without background illumination are presented. This material is available free of charge via the Internet at http://pubs.acs.org.

■ AUTHOR INFORMATION

Notes

The authors declare no competing financial interest.

■ ACKNOWLEDGMENTS

The authors thank Prof. David Norris for access to the SEM and Cary 5E and gratefully acknowledge funding from an ETH Research Grant and from the Swiss National Science Foundation through the Quantum Science and Technology NCCR and an independent research grant. TEM measurements were performed at the Scientific Center for Optical and Electron Microscopy (ScopeM) of ETH Zurich.

■ REFERENCES

(1) Talapin, D. V.; Lee, J.-S.; Kovalenko, M. V.; Shevchenko, E. V. Prospects of Colloidal Nanocrystals for Electronic and Optoelectronic Applications. *Chem. Rev.* **2010**, *110*, 389−458.

(2) Liu, Y.; Gibbs, M.; Puthussery, J.; Gaik, S.; Ihly, R.; Hillhouse, H. W.; Law, M. Dependence of Carrier Mobility on Nanocrystal Size and Ligand Length in PbSe Nanocrystal Solids. *Nano Lett.* **2010**, *10*, 1960−1969.

(3) Kang, M. S.; Sahu, A.; Norris, D. J.; Frisbie, C. D. Size-Dependent Electrical Transport in CdSe Nanocrystal Thin Films. *Nano Lett.* **2010**, *10*, 3727−3732.

(4) Kang, M. S.; Sahu, A.; Norris, D. J.; Frisbie, C. D. Size- and Temperature-Dependent Charge Transport in PbSe Nanocrystal Thin Films. *Nano Lett.* **2011**, *11*, 3887−3892.

(5) Brown, P. R.; Kim, D.; Lunt, R. R.; Zhao, N.; Bawendi, M. G.; Grossman, J. C.; Bulović, V. Energy Level Modification in Lead Sulfide Quantum Dot Thin Films through Ligand Exchange. *ACS Nano* **2014**, *8*, 5863−5872.

(6) Shabaev, A.; Efros, A. L.; Efros, A. L. Dark and Photo-Conductivity in Ordered Array of Nanocrystals. *Nano Lett.* **2013**, *13*, 5454−5461.

(7) Guyot-Sionnest, P. Electrical Transport in Colloidal Quantum Dot Films. *J. Phys. Chem. Lett.* **2012**, *3*, 1169−1175.

(8) Spear, W. The Study of Transport and Related Properties of Amorphous Silicon by Transient Experiments. *J. Non-Cryst. Solids* **1983**, *60*, 1−14.

(9) Marshall, J. M. Carrier Diffusion in Amorphous Semiconductors. *Rep. Prog. Phys.* **1983**, *46*, 1235−1282.

(10) Comber, P. Le; Spear, W. Electronic Transport in Amorphous Silicon Films. *Phys. Rev. Lett.* **1970**, *25*, 1968−1970.

(11) Tiedje, T.; Cebulka, J.; Morel, D.; Abeles, B. Evidence for Exponential Band Tails in Amorphous Silicon Hydride. *Phys. Rev. Lett.* **1981**, *46*, 1425−1428.

(12) Campbell, I. H.; Smith, D. L.; Neef, C. J.; Ferraris, J. P. Consistent Time-of-Flight Mobility Measurements and Polymer Light-Emitting Diode Current−Voltage Characteristics. *Appl. Phys. Lett.* **1999**, *74*, 2809.

(13) Naka, S.; Okada, H.; Onnagawa, H.; Tsutsui, T. High Electron Mobility in Bathophenanthroline. *Appl. Phys. Lett.* **2000**, *76*, 197.

(14) Ip, A. H.; Thon, S. M.; Hoogland, S.; Voznyy, O.; Zhitomirsky, D.; Debnath, R.; Levina, L.; et al. Hybrid Passivated Colloidal Quantum Dot Solids. *Nat. Nanotechnol.* **2012**, *7*, 577−582.

(15) Pattantyus-abraham, A. G.; Kramer, K. I. J.; Barkhouse, K. A. R.; Wang, X.; Konstantatos, G.; Debnath, R.; Levina, L.; et al. Depleted-Heterojunction Colloidal Quantum Dot Solar Cells. *ACS Nano* **2010**, *4*, 3374−3380.

(16) Maraghechi, P.; Labelle, A. J.; Kirmani, A. R.; Lan, X.; Adachi, M. M.; Thon, S. M.; Hoogland, S.; et al. The Donor-Supply Electrode Enhances Performance in Colloidal Quantum Dot Solar Cells. *ACS Nano* **2013**, *7*, 6111−6116.

(17) Würfel, P. *Physics of Solar Cells*; Wiley-VCH Verlag GmbH: Weinheim, Germany, 2005.

(18) Erslev, P. T.; Chen, H.-Y.; Gao, J.; Beard, M. C.; Frank, A. J.; Van de Lagemaat, J.; Johnson, J. C.; et al. Sharp Exponential Band Tails in Highly Disordered Lead Sulfide Quantum Dot Arrays. *Phys. Rev. B* **2012**, *86*, 155313.

(19) Talgorn, E.; Gao, Y.; Aerts, M.; Kunneman, L. T.; Schins, J. M.; Savenije, T. J.; Van Huis, M. a.; et al. Unity Quantum Yield of Photogenerated Charges and Band-Like Transport in Quantum-Dot Solids. *Nat. Nanotechnol.* **2011**, *6*, 733−739.

(20) Choi, J.-H.; Fafarman, A. T.; Oh, S. J.; Ko, D.-K.; Kim, D. K.; Diroll, B. T.; Muramoto, S.; et al. Bandlike Transport in Strongly Coupled and Doped Quantum Dot Solids: A Route to High-Performance Thin-Film Electronics. *Nano Lett.* **2012**, *12* (5), 2631−2638.

(21) Wehrenberg, B. L.; Yu, D.; Ma, J.; Guyot-Sionnest, P. Conduction in Charged PbSe Nanocrystal Films. *J. Phys. Chem. B* **2005**, *109*, 20192−20199.

(22) Romero, H.; Drndic, M. Coulomb Blockade and Hopping Conduction in PbSe Quantum Dots. *Phys. Rev. Lett.* **2005**, *95*, 156801.

(23) Liu, H.; Pourret, A.; Guyot-sionnest, P. Mott and Efros−Shklovskii Variable Range Hopping in CdSe Quantum Dots Films. *ACS Nano* **2010**, *4*, 5211−5216.

(24) Chu, I.-H.; Radulaski, M.; Vukmirovic, N.; Cheng, H.-P.; Wang, L.-W. Charge Transport in a Quantum Dot Supercrystal. *J. Phys. Chem. C* **2011**, *115*, 21409−21415.

(25) Schmidlin, F. Theory of Trap-Controlled Transient Photo-conduction. *Phys. Rev. B* **1977**, *16*, 2362−2385.

(26) Noolandi, J. Equivalence of Multiple-Trapping Model and Time-Dependent Random Walk. *Phys. Rev. B* **1977**, *16*, 4474−4479.

(27) Scher, H.; Montroll, E. Anomalous Transit-Time Dispersion in Amorphous Solids. *Phys. Rev. B* **1975**, *12*, 2455−2477.
(28) Hetsch, F.; Zhao, N.; Kershaw, S. V.; Rogach, A. L. Quantum Dot Field Effect Transistors. *Mater. Today* **2013**, *16*, 312−325.
(29) Osedach, T. P.; Zhao, N.; Andrew, T. L.; Brown, P. R.; Wanger, D. D.; Strasfeld, D. B.; Chang, L.; et al. Treated PbS Quantum Dot Field-Effect Transistors. *ACS Nano* **2012**, *6*, 3121−3127.
(30) Zhitomirsky, D.; Furukawa, M.; Tang, J.; Stadler, P.; Hoogland, S.; Voznyy, O.; Liu, H.; et al. N-type Colloidal-Quantum-Dot Solids for Photovoltaics. *Adv. Mater.* **2012**, *24*, 6181−6185.
(31) Klem, E. J. D.; Shukla, H.; Hinds, S.; MacNeil, D. D.; Levina, L.; Sargent, E. H. Impact of Dithiol Treatment and Air Annealing on the Conductivity, Mobility, and Hole Density in Pbs Colloidal Quantum Dot Solids. *Appl. Phys. Lett.* **2008**, *92*, 212105.
(32) Bozyigit, D.; Volk, S.; Yarema, O.; Wood, V. Quantification of Deep Traps in Nanocrystal Solids, Their Electronic Properties, and Their Influence on Device Behavior. *Nano Lett.* **2013**, *13*, 5284−5288.
(33) Bozyigit, D.; Jakob, M.; Yarema, O.; Wood, V. Deep Level Transient Spectroscopy (DLTS) on Colloidal-Synthesized Nanocrystal Solids. *ACS Appl. Mater. Interfaces* **2013**, *5*, 2915−2919.
(34) Bozyigit, D.; Wood, V. Electrical Characterization of Nanocrystal Solids. *J. Mater. Chem. C* **2014**, *2*, 3172.
(35) Nagpal, P.; Klimov, V. I. Role of Mid-Gap States in Charge Transport and Photoconductivity in Semiconductor Nanocrystal Films. *Nat. Commun.* **2011**, *2*, 486.
(36) Stallinga, P. *Electrical Characterization of Organic Electronic Materials and Devices*; John Wiley & Sons, Ltd: Cornwall, U.K., 2009.
(37) Brinza, M.; Adriaenssens, G. J. The Time-of-Flight Photocurrent Analysis Revisited. *J. Optoelectron Adv. Mater.* **2006**, *8*, 2028−2034.
(38) Hines, M. a.; Scholes, G. D. Colloidal PbS Nanocrystals with Size-Tunable Near-Infrared Emission: Observation of Post-Synthesis Self-Narrowing of the Particle Size Distribution. *Adv. Mater.* **2003**, *15*, 1844−1849.
(39) Preier, H. Recent Advances in Lead-Chalcogenide Diode Lasers. *Appl. Phys. A* **1979**, *20*, 189−206.